

<https://doi.org/10.1038/s43246-024-00481-9>

Local tuning of Rydberg exciton energies in nanofabricated Cu₂O pillars

Check for updates

Anindya Sundar Paul^{1,2,3,5}, Sai Kiran Rajendran¹ , David Ziemkiewicz^{4,5}, Thomas Volz^{2,3} & Hamid Ohadi¹

Rydberg excitons in Cu₂O feature giant optical nonlinearities. To exploit these nonlinearities for quantum applications, the confinement must match the Rydberg blockade size, which in Cu₂O could be as large as a few microns. Here, in a top-down approach, we show how exciton confinement can be realised by focused-ion-beam etching of a polished bulk Cu₂O crystal without noticeable degradation of the excitonic properties. The etching of the crystal to micron sizes allows for tuning the energies of Rydberg excitons locally, and precisely, by optically induced temperature change. These results pave the way for exploiting the large nonlinearities of Rydberg excitons in micropillars for making non-classical light sources, while the precise tuning of their emission energy opens up a viable pathway for realising a scalable photonic quantum simulation platform.

In the last couple of decades, many candidate systems for performing quantum simulations have been investigated including ultracold (Rydberg) atoms in optical lattices or cavities, trapped ions or electrons, and superconducting circuits^{1–3}. A key advantage of Rydberg atom-mediated quantum simulation is that the long-range dipole-dipole interaction strength scales favourably with their principal quantum numbers⁴, enabling access to the strongly interacting, hence, strongly correlated regime. While there has been significant progress in Rydberg atom quantum technologies⁵, a solid-state Rydberg platform with reduced technical overhead and better integration capability is more desirable. Solid state systems provide a robust and miniaturised alternative, where the samples are usually in sub-mm dimensions and can fit inside a very compact experimental setup. This allows for easy tuning and control of the individual excitons and can also be easily scaled. An additional feature of solid-state platforms is their driven-dissipative nature that enables easy access to non-equilibrium physics⁶.

Only recently, high principal quantum number Rydberg excitons up to $n = 30$ have been demonstrated in a Cu₂O crystal^{7–9} with exponentially scaling properties¹⁰. This platform provides an excellent opportunity to explore the feasibility of solid-state quantum simulators based on Rydberg excitons as they exceed micron dimensions. Two interactions in Rydberg excitons of Cu₂O are the Rydberg blockade^{7,11} and plasma blockade¹² effects. One requirement in this direction is the ability to confine two or more Rydberg excitons within their blockade volume and modulate their interaction with each other. Non-linear interactions in excitons can also be mediated through strong light-matter coupling¹³ leading to single particle

quantum interaction^{14,15}. Low n Rydberg exciton-polaritons have been demonstrated with perovskites¹⁶, TMDCs¹⁷, and in Cu₂O up to $n = 6$ ¹⁸. The confinement of the excitons can be demonstrated by two means—optically inducing a potential^{19,20} to trap the excitons, or by means of spatial confinement^{21,22} by creating micro-/nano-structures. While working with optical confinement is experimentally simpler, it lacks resolution when it comes to creating the potential as it cannot go down to submicron levels. On top of that, the potential in itself is quite weak, leading to reduced coherence time for interaction. Creating spatial confinement circumvents both issues by going below the sub-wavelength regime using a focused ion beam (FIB) etching technique²³. While cavity polaritons are better coupled to light for optical transmission, we focus our attention to tuning the properties of Rydberg excitons through spatial confinement. There are two major methods for microfabrication, viz., bottom-up and top-down approaches. Under bottom-up methods, Cu₂O crystals have been grown by melting²⁴, electrodeposition²⁵, sputtering^{26,27}, thermal oxidation²⁸, and e-beam evaporation²⁹. Despite the tremendous progress, synthetic Cu₂O has been found to demonstrate a high density of defects³⁰ and impurities that reduce the visibility of a high quantum number Rydberg excitons⁸. In our top-down approach, we start with a high-quality natural Cu₂O crystal, thin and polish it down, and etch out microstructures using the FIB technique. Other methods of etching semiconductors include: metal-assisted chemical etching³¹ and focused electron beam induced etching^{32,33}.

In this work, we fabricate square micropillars that are 70 microns deep with different lateral cross-sectional areas using FIB etching technique. This

¹SUPA, School of Physics and Astronomy, University of St. Andrews, St. Andrews KY16 9SS, UK. ²Department of Physics and Astronomy, Macquarie University, Sydney, NSW, Australia. ³ARC Centre of Excellence for Engineered Quantum Systems, Macquarie University, Sydney, NSW, Australia. ⁴Institute of Mathematics and Physics, Technical University of Bydgoszcz, Al. Prof. S. Kaliskiego 7, 85-789 Bydgoszcz, Poland. ⁵These authors contributed equally: Anindya Sundar Paul, David Ziemkiewicz. e-mail: skr7@st-andrews.ac.uk; ho35@st-andrews.ac.uk

allows us to investigate the properties of the *yellow 1s* ortho-excitons and the yellow *np* excitons through photoluminescence (PL) studies. While PL of excitons in Cu_2O has been widely investigated, properties of bulk Cu_2O can be significantly different from that of nanostructures. Other studies on Cu_2O nano- and microparticles only investigate the average properties of an ensemble^{29,34}. Here, for the first time, we demonstrate a size-dependent tuning of exciton properties within one microstructure at a time.

Results and discussions

Fabrication of micropillars

FIB etching has been used to micromachine nanostructures on metallic contacts and silicon in the manufacturing of semiconductor chips, as well as the preparation of samples for transmission electron microscopy. Gallium ions are the standard source material for this technique due to their easy melting and focusing using a high-voltage electrostatically charged tip. Gallium atoms are also heavy and enable faster sputtering rates of the target materials using elastic and inelastic collisions.

Here, we use this technique to etch pillars on a bulk crystal of Cu_2O (see “Methods” for details on crystal preparation). With incident gallium ions accelerated through 30 kV, the etching rate is about $200 \mu\text{m}^3$ per minute at 3 nA current. In order to have a $2.5 \mu\text{m}$ separation around a $5 \mu\text{m} \times 5 \mu\text{m}$ pillar, a lateral area of $75 \mu\text{m}^2$ would need to be etched. Setting the depth to be $70 \mu\text{m}$, it takes about half an hour to etch out this required region. While attempting pillars of smaller lateral area, it was found that as the ion beam etches deep into the sample, the conical shape of the beam also results in etching away the top surface of the pillar resulting in a tapered pillar. While the size of the cone can be reduced by etching at a lower ion current of 300 pA, this would require an etching time of 5 h for one nanopillar. Therefore, a 3 nA was chosen as the optimum current to etch a sufficient number of pillars.

Four different pillars are etched by leaving different exclusion zones at the centre of a $10 \mu\text{m} \times 10 \mu\text{m} \times 70 \mu\text{m}$ volume. The exclusion zones for pillars A, B, C, and D are squares of $5 \mu\text{m} \times 5 \mu\text{m}$, $4 \mu\text{m} \times 4 \mu\text{m}$, $3 \mu\text{m} \times 3 \mu\text{m}$, and $2 \mu\text{m} \times 2 \mu\text{m}$, respectively. Etching of the region around the exclusion zone is performed in steps of four of rectangular cross-sectional regions, one for each side of the pillar. Each cross-section is etched using a raster multi-pass scan such that the etching would end at the edge closest to the pillar during each scan (see Fig. 1a). This ensures that any material redeposited close to the pillars during the sputtering process will be removed at the end of each pass. As can be seen in the electron microscopy images (Fig. 1b), while the dimension at the bottom of the pillars is close to the designed ones, the pillars taper at the top with pillar D resulting in a very small tip of $1.6 \times 1.0 \mu\text{m}^2$ area. In the remaining part of this work, we investigate the PL from these four pillars at 4 K temperature.

PL at low powers

Here, we study the lowest energy excitons in Cu_2O (the so-called yellow series). They originate from the $\Gamma_7^+ \rightarrow \Gamma_6^+$ transition³⁵ with a bandgap energy of 2.17 eV. The brightest transition is the quadrupole *1s* ortho-exciton transition at 2.03 eV and a broad phonon replica at 2.02 eV. The p-exciton Rydberg series starts with the principal quantum number $n = 2$ at 2.14 eV. PL for *np* excitons has been observed up to $n = 10$ previously³⁶. Here, we observe PL (see Fig. 1c) from *1s* and *np* excitons up to $n = 6$ both in the bulk crystal region and in the micropillars (see “Methods” for more details). This observation on its own is important because it shows that, at least for PL, the bulk of the crystal has stayed intact during the etching process.

Laser power dependence

As the laser power increased, we observed two distinct trends (see Fig. 2). Firstly, both *np* Rydberg and *1s* ortho-excitons exhibit a clear redshift of PL energy with an increase in incident laser power for all pillars. The redshift becomes more dramatic as the dimensions of the pillars become smaller. This energy shift with power for the smallest pillar is ~ 14 times larger than the bulk. This redshift is due to the temperature increase of the crystal by the

high absorption of laser power resulting in shifting of the energy bandgap³⁷. Another feature is the splitting in the PL spectra at higher powers, strikingly similar to what has been reported due to mechanical stress³⁸. While one may attribute the splitting to local strain from the large temperature gradient

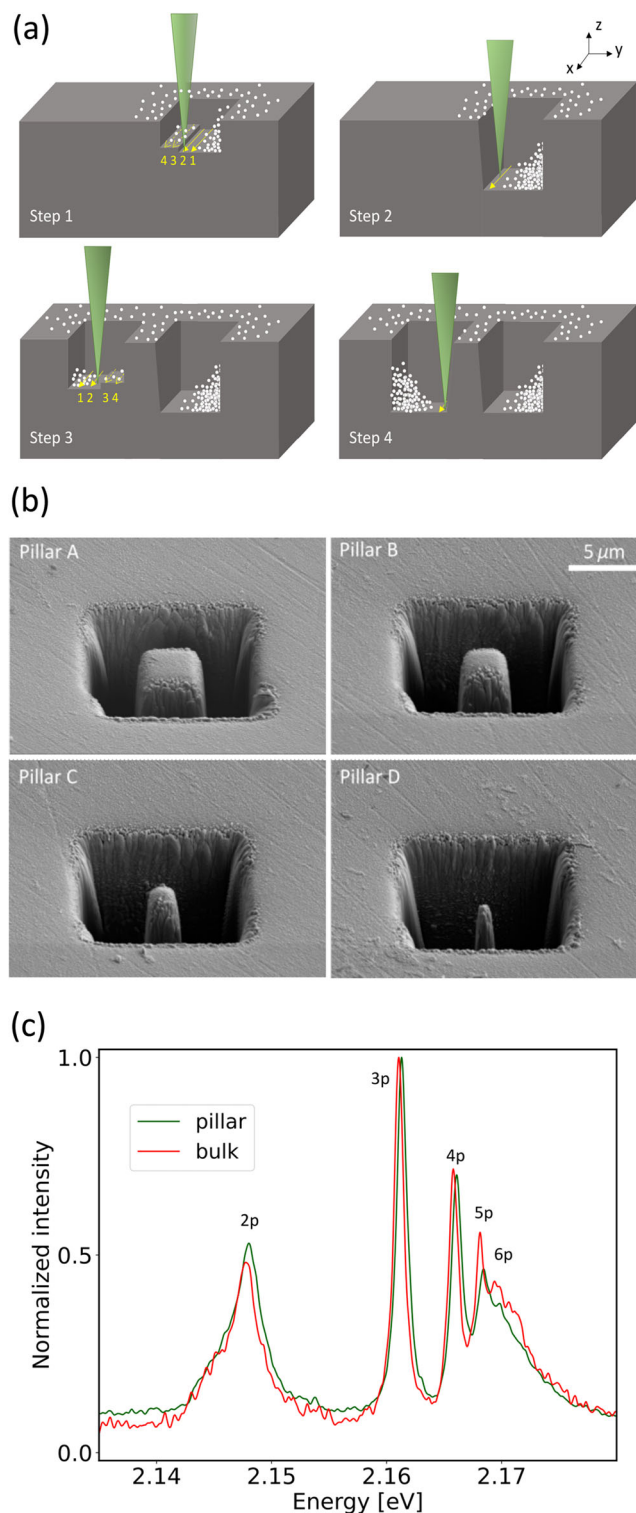


Fig. 1 | Fabrication of the pillars and their PL spectra at low laser power. **a** Steps taken in FIB fabrication of pillars to minimise redeposition (shown in white) on pillars. **b** SEM images of the four micropillars constructed using FIB technique. The actual dimensions of the pillars are: A: $4.4 \times 4.0 \mu\text{m}^2$, B: $3.5 \times 4.3 \mu\text{m}^2$, C: $2.7 \times 2.0 \mu\text{m}^2$, and D: $1.6 \times 1.0 \mu\text{m}^2$. **c** PL spectra of the sample for pillar B (green) and a bulk position on the crystal (red) showing Rydberg excitons up to $n = 6$ at low optical excitation power of 1.68 mW and the cryostat temperature $T = 4 \text{ K}$.

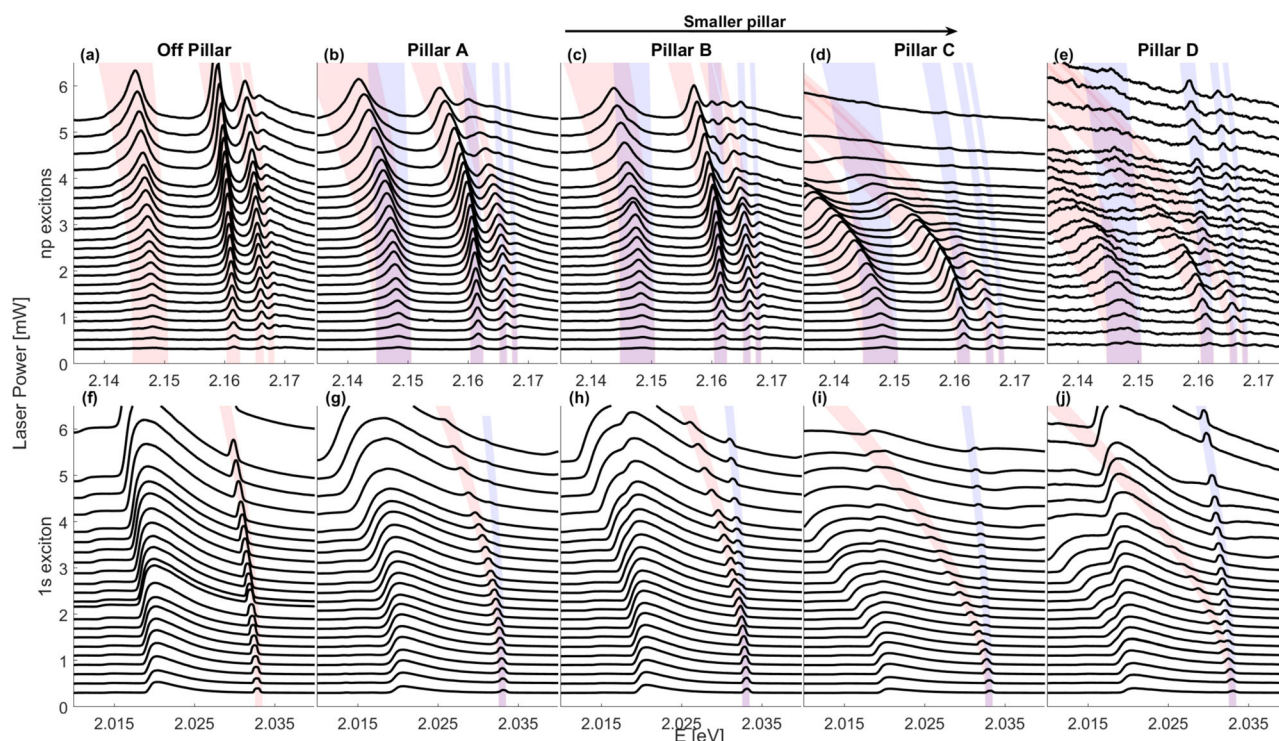


Fig. 2 | PL spectra of all the pillars and off-pillar data for np excitons and $1s$ excitons with increasing laser power and decreasing dimensions of the pillars. Plots (b) to (e) show the trend in the np excitons as the size of the pillars decreases, while plots (g) to (j) show the trend for $1s$ ortho-excitons. In both cases, the ‘splitting’ becomes more prominent with the decreasing size of the pillars, and starts to appear

with lower laser powers as well. Red/blue areas mark estimated positions and line widths of PL peaks originating from hot/cold parts of the sample. In the case of the off-pillar measurements as seen in plots (a) and (f), no splitting is visible since all the power is absorbed in the hot region. All measurements were performed at the cryostat temperature $T = 4$ K.

along the long axis of the pillar, we investigate this source using simulations that estimate the temperature gradient and the resultant strain.

Estimation of crystal temperature

We make some preliminary estimations on the expected pillar temperature and compare it with the absorbed laser power. For pillar A, we have the following characteristics: (i) volume: $4.3 \times 4.8 \times 70 \mu\text{m}^3$, (ii) cross-section/top area: $20.6 \mu\text{m}^2$ (note that pillar is slightly tapered towards the top, which we neglect here since we don’t have a good measurement of the bottom cross-section), (iii) side area: $640 \mu\text{m}^2$ (again, due to the fact that it is getting wider towards the bottom, this value is underestimated), (iv) top temperature: $T = 100$ K at 8 mW (approximate value derived from the observed band gap shift).

For Cu_2O , the relative permittivity is $\epsilon_r = 7.5$, so the refractive index is $n = 2.74$, and transmission at normal incidence is $T = 1 - \left(\frac{n-1}{n+1}\right)^2 \simeq 0.78$. For an 8 mW incident beam, the absorbed power is $P \simeq 6.3$ mW. On including the total transmission coefficient of the microscope objective and cryostat window of 0.7, and the curved surface of the pillar top increasing the reflection coefficient, we estimate the actual absorbed power is of the order of ~ 1 mW. We now consider the two primary ways of dissipating the absorbed energy.

Thermal radiation. Using the Stefan-Boltzmann law the energy flux is $j = \epsilon\sigma T^4 = 2.835 \text{ Wm}^{-2}$, where $\sigma = 5.670 \times 10^{-8} \text{ Wm}^{-2}\text{K}^{-4}$ is the Stefan-Boltzmann constant, and we obtained an emissivity $\epsilon \sim 0.5$. Overall, $0 < \epsilon < 1$, and as we are only interested in estimating the order of magnitude, the thermal radiation is negligible even for $\epsilon = 1$. From the entire pillar surface area, we obtain a radiated power of $P_R = 1.86 \times 10^{-6}$ mW. This is negligible compared to the power absorbed by the laser.

Thermal conduction. As an approximation, we take the pillar to be of a constant cross-section through its length and that the bulk material in

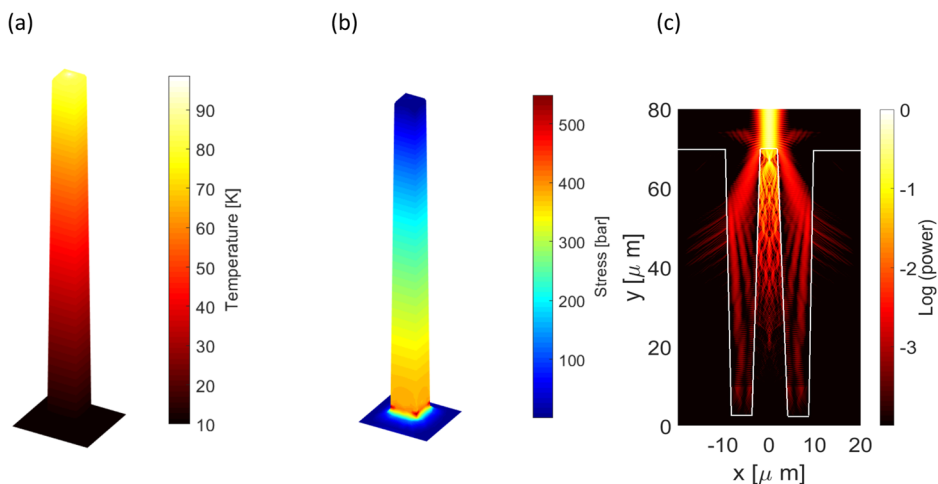
contact with its base has nearly the same temperature as the thermostat, e.g. $T < 10$ K. Across the pillar, there is a temperature gradient of $\Delta T/L = 1.4 \times 10^6 \text{ Km}^{-1}$. Using the thermal conductivity of Cu_2O as approximately the same as CuO ³⁹ $K = 30 \text{ Wm}^{-1}\text{K}^{-1}$ the heat flux is $j = K\Delta T/L = 42.8 \times 10^6 \text{ Wm}^{-2}$. For a cross-sectional area of $S = 20.6 \times 10^{-12} \text{ m}^2$ we obtain a power of $P \simeq 0.9$ mW. This is close to the absorbed power of 1 mW. Our assumption of the temperature gradient to be parallel to the axis of the pillar is justified by the smaller diameter of the pillar compared to its length, and a laser spot size ($3 \mu\text{m}$) which covers most of the pillar top surface. Therefore, we can expect a linear gradient of the temperature along the pillar length. To verify this, we have performed finite element analysis of the thermal conduction (see Fig. 3) and find that the variance of temperature across the top face is within 10 K and the heating at the base of the pillar is negligible.

On strain due to temperature gradient

To obtain temperature distribution, we use thermal expansion and Young’s modulus of Cu_2O , $E = 100 \text{ GPa}$ ⁴⁰ to estimate stress in the pillars. Using the finite element modelling, we obtain the stress distribution shown in Fig. 3b.

As expected, the highest stress occurs at the corners of the base, which are stress concentration points. The peak value obtained in simulation is about 530 bar (53 MPa), although it should be mentioned that this value depends on the radius of curvature of the base which is not known. The top face is mostly stress-free, with a maximum value of ~ 30 bar. As shown in previous results³⁸, a pressure of 2000 bar would be needed to be applied in order to observe a 10 meV shift. With only 30 bar temperature-related stress at the top of the pillar, the shift in the spectra would be on the order of μeV . This value is smaller than the resolution of our spectrometer. To ensure that, we can analyse the fitting error of the formula (1) to the pillar and off-pillar data; if any stress-related effects are present, they should be different in these two cases. The results show no difference (see Supplementary Fig. S1).

Fig. 3 | Temperature and stress distribution simulation for pillar A. **a** FEM analysis results for Pillar A, assuming the top temperature of 100 K. **b** Stress distribution of the pillar due to thermal expansion. **c** FDTD simulation result of beam propagation; time-averaged energy density $\rho = \epsilon E^2$ is calculated.



Thus we conclude that the stress levels are not sufficient to produce a noticeable shift in exciton energy.

Origin of splitting in PL spectra

Using the above heating model we estimate the source of ‘hot’ and ‘cold’ bands in the PL spectrum (see Fig. 2). We rule out the possibility of having cold regions of significant size on the top face of the pillar that would result in a detectable PL level. The observed lines originating from cold regions could be emitted either from pillar sides or its surrounding implying that a significant fraction of illuminating laser power is not absorbed by the top face. To investigate this issue, we use the FDTD method to simulate wave propagation in the system. Since we are only interested in some general characteristics of the system, a two-dimensional simulation is used where a cross-section of the geometry is investigated. Since the pillar size (3 μm) is approximately 5 times larger than the wavelength, the assumption that the system is much larger than the wavelength in the direction perpendicular to the cross-section plane is reasonable.

The FDTD simulation shows several interesting features in the calculated energy density distribution (see Fig. 3c). The vertical beam is reflected from the pillar top, which can be seen as two small “wings” on the sides of the beam. Their cutoff near $y = 75 \mu\text{m}$ is a result of absorbing layers placed in the simulation to avoid stray reflections. Due to the limited simulation space, the radiation source is placed close to the pillar top at $y = 80 \mu\text{m}$; reflections between the source and pillar top result in a standing wave pattern across the beam. A key result is the diffraction of the incident beam which results in two side lobes propagating at an angle of approximately 30 degrees to the pillar and hitting the trench walls. Since this power density is approximately 10–20 times smaller than in the beam centre at the top face, they do not result in any appreciable heating. However, these side beams illuminating side walls and the bottom comprise a significantly larger area than the pillar top. This results in a non-negligible PL signal from these cold regions. The exact shape of cold emission regions is not well known, as it depends on the precise angle of the trench and pillar walls, which could be only roughly estimated from SEM images. Another interesting feature is the fact that the rounded pillar top seems to act as a lens, focusing the beam to a spot a few μm under the surface. This would suggest that with sufficient sensitivity, one could see a heavily red-shifted PL band originating from the small but hot spot at the focus.

Exciton energy tuning with laser power

To further study the effect of temperature and to validate our theoretical model of band gap energy shift, we have performed a temperature sweep scan where a series of PL spectra have been measured at constant laser power

while varying the cryostat temperature. For the theoretical $E_g(T)$ dependence, we use the so-called Varshni formula⁴¹:

$$E_g = E_{g_0} - \frac{\alpha T^2}{\beta + T}, \quad (1)$$

where α, β are fitting parameters of a particular material. Based on data by Snoko et al.⁴², we obtain values for $\alpha = 4.8 \times 10^{-4} \text{ eVK}^{-1}$ and $\beta = 275 \text{ K}$. By fitting the above model to the recent experimental data by Malerba et al. values for⁴³, we obtain $\alpha = 6.125 \times 10^{-4} \text{ eVK}^{-1}$ and $\beta = 375.57 \text{ K}$. Despite apparent large disagreement between values, the difference between models is only 0.08 meV at $T = 100 \text{ K}$ and scales approximately as T^2 . A laser power $P = 1 \text{ mW}$ results in approximately 15 K of heating from the cryostat temperature according to the observed energy shift. With this correction, we get an excellent agreement with theoretical relation (see Supplementary Fig. S1).

Another temperature-dependent parameter is spectral linewidth. We use the theoretical relation⁴⁴

$$\Gamma(n) = \Gamma_0(n) + \gamma_{AC}T + \gamma_{LO} \left(e^{\omega_{LO}/kT} - 1 \right)^{-1}, \quad (2)$$

with constants γ_{AC}, γ_{LO} representing acoustic phonons and LO phonons. The value $\Gamma_0(n)$ is the linewidth of the excitonic state with principal number n , in the limit of low temperature, taken from fitting to the experimental data⁷. The comparison of measured line widths with the theoretical prediction is shown in Supplementary Fig. S2.

There is an excellent match with the data from Kang et al.³⁷. In our results, there is a constant broadening of about 0.3 meV. This broadening could be due to the lower quality of our sample as well as the overlap of multiple lines corresponding to confinement states⁴⁵.

Using the relation between the bandgap shift with crystal temperature, we can estimate the hottest temperature of the pillars for a given laser power. The power dependence of the energy shift of 2p excitons in pillars shows a quadratic dependence with laser power (see Fig. 4a). Since the bandgap redshift has a quadratic relation with temperature, it follows that the temperature of the pillar varies linearly with incident laser power (see Fig. 4b). The effective temperature of the exciton can be determined by fitting the 1s ortho-exciton phonon replica (see Supplementary Fig. S3). The resulting effective temperature trend is consistent with the temperatures extracted using the Varshni formula, except for a noticeable offset. This discrepancy is attributed to the sample’s elevated temperature relative to the coldfinger (see Supplementary Fig. S4). The PL intensity per unit area of the pillar tips for 2p exciton for all pillars follows a super-linear fit $aP^{1.5}$, with the excitation laser power P (Fig. 5). The fall-offs from the

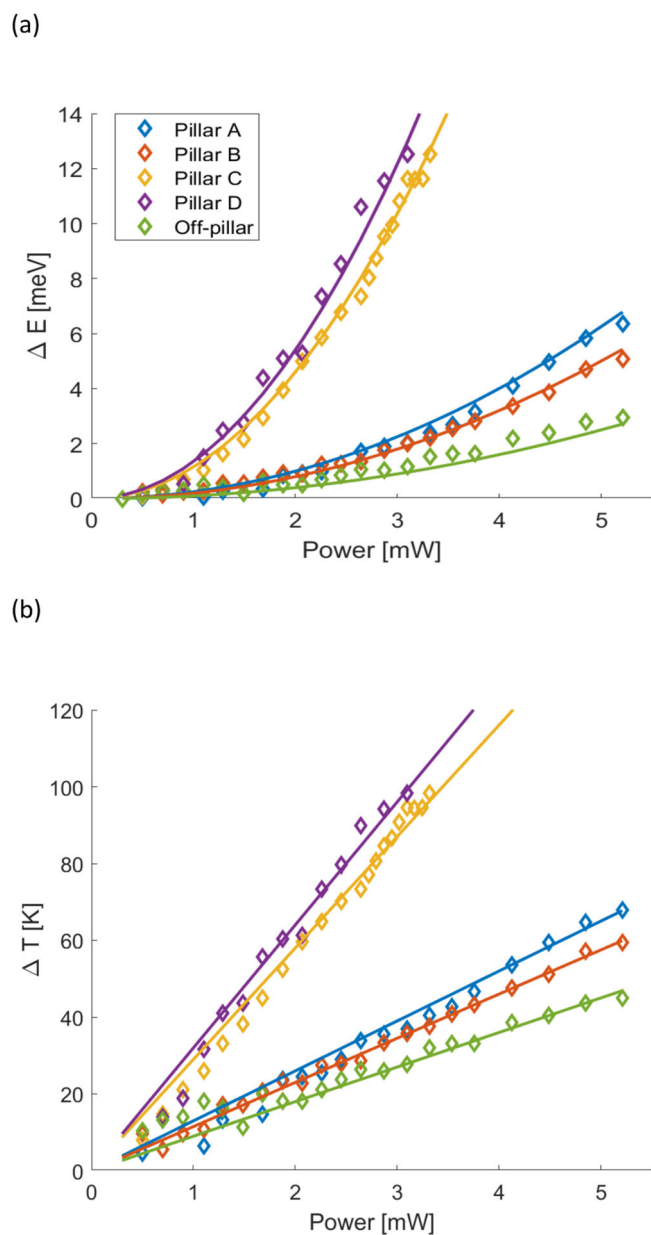


Fig. 4 | Energy shifts of 2p excitons and their corresponding temperature estimates. **a** Energy shift of 2p excitons for all the pillars and a bulk position on the sample. They follow a quadratic fit $\Delta E = aP^2$ with power P , where $a = [0.1, 0.25, 0.2, 1.15, 1.35]$ eV K^{-1} for the bulk, pillar A, B, C, D respectively. **b** The temperature estimates are plotted based on the energy shift. They follow a linear fit $T = bP$ with power, where $b = [9, 13, 11.5, 29, 32]$ K mW^{-1} for the bulk, pillar A, B, C, D.

trend are consistent with the thermal ionization of the excitons, which leads to the energy being redshifted, as seen in Fig. 4a. The effect is more discernible in smaller pillars, as they heat more with the same laser power. The trend is similar for 3p excitons, but with an earlier fall-off from the super-linear trend as they are closer to the bandgap and their binding energy is smaller.

The capability to locally tune the energies of the excitonic states by changing the bandgap energy using optical means is a simple yet powerful tool for lattices made from these pillars²¹. This simple and versatile technique has significant advantages over the previously existing methods like external electric field⁴⁶, magnetic field⁴⁷, or strain³⁸. Local tuning of energy is possible with electric fields and strain. Achieving strain in a micron scale is challenging and tunability with electric fields is too small. Both methods inhibit higher-lying excitons due to the broadening of transitions and

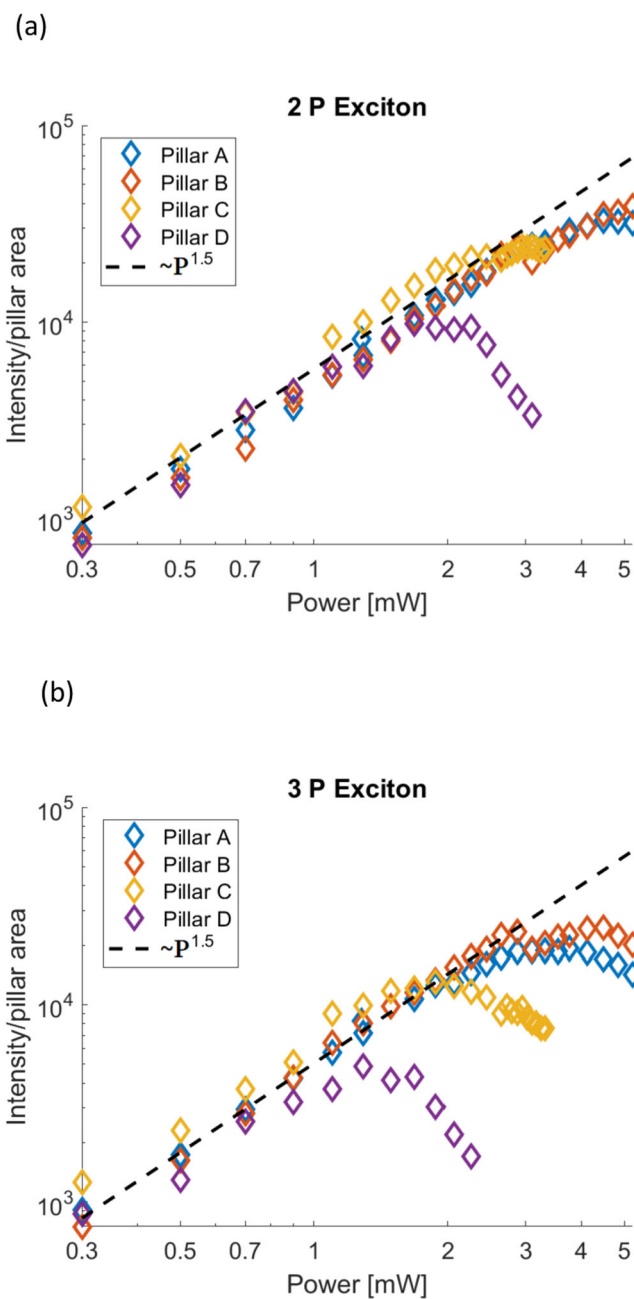


Fig. 5 | Laser power dependence of pillars' PL intensity. **a** Power dependence of the PL intensity per unit area of the pillar tips for 2p exciton **(a)** and 3p excitons **(b)** follows a superlinear fit followed by a sudden fall off.

ionization¹⁰. None of these three methods have shown local tuning of energies to the order of 10 meV as demonstrated here.

Conclusion

In conclusion, we have successfully fabricated microstructures from the bulk Cu_2O , whilst preserving their excitonic properties. The micropillars show PL for $1s$ ortho-excitons and np Rydberg excitons up to $n = 6$. We can locally tune the energy of the excitons in the pillar by changing the power of the laser. The non-resonant absorption of the laser power induces a local temperature change, which locally shifts the band gap of the crystal. The microstructures demonstrated here could be used for studying single-photon optical nonlinearities^{48,49}. The local tuning of exciton energies is a useful tool to circumvent disorder for the realisation of strongly correlated lattices of Rydberg polaritons⁵⁰.

Methods

Crystal preparation

We first start with a naturally mined crystal of Cu_2O . We cut the crystal along one of the crystallographic planes, and manually thin down and polish both surfaces using sheets of different grit sizes. The thinned sample (~70 μm thick) is then mounted on a CaF_2 substrate using a UV-cured epoxy owing to its excellent cryogenic thermal conductivity.

FIB fabrication

The micropillars were etched using an FEI Scios Dual-beam system. In order to etch microstructures using FIB, it is necessary to electrically ground the surface of the material in order to discharge the implanted beam of ions. As neither Cu_2O nor CaF_2 substrate is a good electrical conductor, a thin line of conductive silver paste is traced from the sample surface to the aluminium chuck at the bottom. The sample is evacuated to low pressures to avoid the formation of a charged atmosphere that could deflect incoming ions. The instrument consists of a vertical electron beam for microscopy and an ion beam at 52 degrees for etching. The sample is elevated to the eucentric point of the dual column beams and then tilted to face the ion beams head-on. A voltage of 30 kV and a low current of 30 pA is chosen to optimise the focus and astigmatism of the ion beams while incident on the sample surface at a high magnification of 5000 \times . It is apparent that even a few seconds of exposing the sample during the alignment to the ion beam is enough to start etching of the sample surface leading to roughening of the entire sample area in view. Therefore, a new surface is chosen for etching our microstructures after the alignment of the electron and ion beams. Since Cu_2O is softer than silicon, the rate of etching a volume is subsequently about 7 times higher.

PL measurements

The sample is mounted in a continuous-flow cryostat and is cooled down to 4 K. We perform PL spectroscopy on individual micropillars using a green continuous wave laser of 520 nm wavelength (Thorlabs PL203) in conjunction with a 550 nm shortpass filter. The laser beam focuses onto a 2 μm diameter spot after passing through a Mitutoyo 20 \times objective lens (NA = 0.42). Filtered emission from the micropillar(s) using a 550 nm longpass filter is collected through the same objective, distributed, and analyzed using a spectrometer (Andor Shamrock 750) coupled to an EMCCD camera (Andor Newton). A CMOS camera (Thorlabs Quantalux) provides a live image of the sample to align the optics and create excitation directly on the micropillars.

FDTD simulation

The performed simulation is based on a standard Yee algorithm⁵¹, where a set of field evolution equations is derived from Maxwell's equations and used to update the electric and magnetic field values within some defined computation domain. The domain is divided by a rectangular grid with a single cell size $\Delta x = 50$ nm, which is a compromise between calculation accuracy and memory demand. For the same reason, a two-dimensional representation of the system with TM field configuration is chosen; the electric field has two components in the plane of the propagation $\mathbf{E} = [E_x, 0, E_z]$, and the magnetic field has a single component perpendicular to the xz plane $\mathbf{H} = [0, H_y, 0]$. Such a representation is valid as long as the size of the system in z axis is much larger than wavelength. In our case, the pillar top size is on the order of 3 μm , as compared to $\lambda \sim 570$ nm. This means that the conditions for accurate simulation are approximately met; we stress that the goal of the simulation is only to get some qualitative insight into EM field distribution.

The full set of equations solved is as follows

$$\frac{\partial H_y}{\partial t} = \frac{1}{\mu_0} \left(\frac{\partial E_x}{\partial z} - \frac{\partial E_z}{\partial x} \right), \quad (3)$$

$$\frac{\partial E_x}{\partial t} = \frac{1}{\epsilon_0 \epsilon} \left(\frac{\partial H_y}{\partial z} + j_x \right), \quad (4)$$

$$\frac{\partial E_z}{\partial t} = \frac{1}{\epsilon_0 \epsilon} \left(\frac{\partial E_x}{\partial z} + j_z \right), \quad (5)$$

where μ_0 , ϵ_0 are the vacuum permittivity and permeability, and j_x, j_z are the components of current density used to introduce a radiation source to the system. We use $\epsilon = 1$ for vacuum and $\epsilon = 7.5$ for Cu_2O .

The equations above are rearranged to obtain evolution equations for E_x, E_z, H_y fields, allowing one to calculate the next field value based on the current one, with some fixed time step Δt .

Data availability

The research data underpinning this publication can be accessed from University of St Andrews Research Data repository <https://doi.org/10.17630/bdc0fa20-1218-4094-9306-3fd372a792d9>⁵².

Received: 8 September 2023; Accepted: 18 March 2024;

Published online: 28 March 2024

References

- Bloch, I., Dalibard, J. & Zwerger, W. Many-body physics with ultracold gases. *Rev. Mod. Phys.* **80**, 885–964 (2008).
- Buluta, I. & Nori, F. Quantum simulators. *Science* **326**, 108–111 (2009).
- Georgescu, I. M., Ashhab, S. & Nori, F. Quantum simulation. *Rev. Mod. Phys.* **86**, 153–185 (2014).
- Saffman, M., Walker, T. G. & Mølmer, K. Quantum information with Rydberg atoms. *Rev. Mod. Phys.* **82**, 2313–2363 (2010).
- Adams, C. S., Pritchard, J. D. & Shaffer, J. P. Rydberg atom quantum technologies. *J. Phys. B: At. Mol. Optical Phys.* **53**, 012002 (2019).
- Carusotto, I. & Ciuti, C. Quantum fluids of light. *Rev. Mod. Phys.* **85**, 299–366 (2013).
- Kazimierzczuk, T., Fröhlich, D., Scheel, S., Stolz, H. & Bayer, M. Giant Rydberg excitons in the copper oxide Cu_2O . *Nature* **514**, 343–347 (2014).
- Heckötter, J., Janas, D., Schwartz, R., Aßmann, M. & Bayer, M. Experimental limitation in extending the exciton series in Cu_2O towards higher principal quantum numbers. *Phys. Rev. B* **101**, 235207 (2020).
- Versteegh, M. A. M. et al. Giant Rydberg excitons in Cu_2O probed by photoluminescence excitation spectroscopy. *Phys. Rev. B* **104**, 245206 (2021).
- Heckötter, J. et al. Scaling laws of Rydberg excitons. *Phys. Rev. B* **96**, 125142 (2017).
- Walther, V., Krüger, S. O., Scheel, S. & Pohl, T. Interactions between Rydberg excitons in Cu_2O . *Phys. Rev. B* **98**, 165201 (2018).
- Heckötter, J. et al. Rydberg excitons in the presence of an ultralow-density electron-hole plasma. *Phys. Rev. Lett.* **121**, 097401 (2018).
- Amo, A. & Bloch, J. Exciton-polaritons in lattices: a non-linear photonic simulator. *Comptes Rendus Phys.* **17**, 934–945 (2016). Polariton physics / Physique des polaritons.
- Muñoz-Matutano, G. et al. Emergence of quantum correlations from interacting fibre-cavity polaritons. *Nat. Mater.* **18**, 213–218 (2019).
- Delteil, A. et al. Towards polariton blockade of confined exciton-polaritons. *Nat. Mater.* **18**, 219–222 (2019).
- Bao, W. et al. Observation of Rydberg exciton polaritons and their condensate in a perovskite cavity. *Proc. Natl Acad. Sci.* **116**, 20274–20279 (2019).
- Gu, J. et al. Enhanced nonlinear interaction of polaritons via excitonic Rydberg states in monolayer WSe_2 . *Nat. Commun.* **12**, 2269 (2021).
- Orfanakis, K. et al. Rydberg exciton-polaritons in a Cu_2O microcavity. *Nat. Mater.* <https://www.nature.com/articles/s41563-022-01230-4> (2022).
- Askitopoulos, A. et al. Polariton condensation in an optically induced two-dimensional potential. *Phys. Rev. B* **88**, 041308 (2013).

20. Orfanakis, K., Tzortzakakis, A. F., Petrosyan, D., Savvidis, P. G. & Ohadi, H. Ultralong temporal coherence in optically trapped exciton-polariton condensates. *Phys. Rev. B* **103**, 235313 (2021).
21. Bajoni, D. et al. Excitonic polaritons in semiconductor micropillars. *Acta Phys. Polonica A* **114**, 933–943 (2008).
22. Bajoni, D. et al. Polariton laser using single micropillar GaAs-GaAlAs semiconductor cavities. *Phys. Rev. Lett.* **100**, 047401 (2008).
23. Seliger, R. L., Ward, J. W., Wang, V. & Kubena, R. L. A high-intensity scanning ion probe with submicrometer spot size. *Appl. Phys. Lett.* **34**, 310–312 (2008).
24. Naka, N., Hashimoto, S. & Ishihara, T. Thin films of single-crystal cuprous oxide grown from the melt. *Jpn. J. Appl. Phys.* **44**, 5096–5101 (2005).
25. Oba, F. et al. Epitaxial growth of cuprous oxide electrodeposited onto semiconductor and metal substrates. *J. Am. Ceram. Soc.* **88**, 253–270 (2005).
26. Yin, Z. et al. Two-dimensional growth of continuous Cu₂O thin films by magnetron sputtering. *Appl. Phys. Lett.* **86**, 061901 (2005).
27. Park, J.-W. et al. Microstructure, optical property, and electronic band structure of cuprous oxide thin films. *J. Appl. Phys.* **110**, 103503 (2011).
28. Mani, S., Jang, J., Ketterson, J. & Park, H. High-quality crystals with various morphologies grown by thermal oxidation. *J. Cryst. Growth* **311**, 3549–3552 (2009).
29. Steinhauer, S. et al. Rydberg excitons in Cu₂O microcrystals grown on a silicon platform. *Commun. Mater.* **1**, 11 (2020).
30. Lynch, S. A. et al. Rydberg excitons in synthetic cuprous oxide Cu₂O. *Phys. Rev. Mater.* **5**, 084602 (2021).
31. Huang, Z., Geyer, N., Werner, P., de Boor, J. & Gösele, U. Metal-assisted chemical etching of silicon: a review. *Adv. Mater.* **23**, 285–308 (2011).
32. Coburn, J. W. & Winters, H. F. Ion- and electron-assisted gas-surface chemistry—an important effect in plasma etching. *J. Appl. Phys.* **50**, 3189–3196 (2008).
33. Randolph, S. J., Fowlkes, J. D. & Rack, P. D. Focused, nanoscale electron-beam-induced deposition and etching. *Crit. Rev. Solid State Mater. Sci.* **31**, 55–89 (2006).
34. Orfanakis, K. et al. Quantum confined Rydberg excitons in Cu₂O nanoparticles. *Phys. Rev. B* **103**, 245426 (2021). Publisher: American Physical Society.
35. Kleinman, L. & Mednick, K. Self-consistent energy bands of Cu₂O. *Phys. Rev. B* **21**, 1549–1553 (1980).
36. Takahata, M. & Naka, N. Photoluminescence properties of the entire excitonic series in Cu₂O. *Phys. Rev. B* **98**, 195205 (2018).
37. Kang, D. D. et al. Temperature study of Rydberg exciton optical properties in Cu₂O. *Phys. Rev. B* **103**, 205203 (2021).
38. Waters, R. G., Pollak, F. H., Bruce, R. H. & Cummins, H. Z. Effects of uniaxial stress on excitons in Cu₂O. *Phys. Rev. B* **21**, 1665–1675 (1980).
39. Abdelmalik, A. & Sadiq, A. Thermal and electrical characterization of composite metal oxides particles from periwinkle shell for dielectric application. *SN Appl. Sci.* **1**, 373 (2019).
40. Jian, S.-R., Chen, G.-J. & Hsu, W.-M. Mechanical properties of Cu₂O thin films by nanoindentation. *Materials* **6**, 4505–4513 (2013).
41. Varshni, Y. P. Temperature dependence of the energy gap in semiconductors. *Physica* **34**, 149–154 (1967).
42. Snoke, D. W., Shields, A. J. & Cardona, M. Phonon-absorption recombination luminescence of room-temperature excitons in Cu₂O. *Phys. Rev. B* **45**, 11693–11697 (1992).
43. Malerba, C. et al. Absorption coefficient of bulk and thin film Cu₂O. *Sol. Energy Mater. Sol. Cells* **95**, 2848–2854 (2011).
44. Zhao, H., Wachter, S. & Kalt, H. Effect of quantum confinement on exciton-phonon interactions. *Phys. Rev. B* **66**, 085337 (2002).
45. Orfanakis, K. et al. Quantum confined Rydberg excitons in Cu₂O nanoparticles. *Phys. Rev. B* **103**, 245426 (2021).
46. Heckötter, J. et al. High-resolution study of the yellow excitons in Cu₂O subject to an electric field. *Phys. Rev. B* **95**, 035210 (2017).
47. Schweiner, F. et al. Magnetoexcitons in cuprous oxide. *Phys. Rev. B* **95**, 035202 (2017).
48. Chang, D. E., Vuletić, V. & Lukin, M. D. Quantum nonlinear optics-photon by photon. *Nat. Photon.* **8**, 685–694 (2014).
49. Khazali, M., Heshami, K. & Simon, C. Single-photon source based on Rydberg exciton blockade. *J. Phys. B: At. Mol. Optical Phys.* **50**, 215301 (2017).
50. Ohadi, H. et al. Synchronization crossover of polariton condensates in weakly disordered lattices. *Phys. Rev. B* **97**, 195109 (2018).
51. Taflove, A., Hagness, S. & Picket-May, M. Computational Electromagnetics: The Finite-Difference Time-Domain Method, 629–670 (Elsevier Inc, 2005).
52. Paul, A. S., Rajendran, S. K., Ziemkiewicz, D., Volz, T. & Ohadi, H. Local tuning of Rydberg exciton energies in nanofabricated Cu₂O pillars (dataset). St Andrews Research Repository. <https://doi.org/10.17630/bdc0fa20-1218-4094-9306-3fd372a792d9> (2024).

Acknowledgements

H.O. thanks Matthew P.A. Jones for helpful discussions. S.K.R. thanks Aaron Naden and David Miller from School of Chemistry, University of St Andrews, for useful discussions on FIB etching techniques. This work was supported by the EPSRC through grant No. EP/S014403/1, by The Royal Society through RGS/R2/192174, and by the Leverhulme Trust through grant No. RPG-2022-188. A.S.P. acknowledges the PhD scholarship from University of St Andrews and Macquarie University and the support of Sydney Quantum Academy, Sydney, NSW, Australia for The SQA Supplementary Scholarship. S.K.R. acknowledges the Carnegie Trust for the Universities of Scotland Research Incentive Grant RIG009823. T.V. acknowledges support through the ARC Centre of Excellence for Engineered Quantum Systems (CE170100009). We acknowledge the support of EPSRC Capital for Great Technologies Grant EP/L017008/1 and the EPSRC Strategic Equipment Resource Grant EP/R023751/1 for the use of the FIB equipment for the fabrication of the pillars.

Author contributions

S.K.R. fabricated the sample. A.S.P. took the measurements. D.Z. analysed the data and performed simulations/theoretical calculations. T.V. and H.O. supervised the project. S.K.R. and H.O. conceived and designed the project. All authors contributed to the writing of the manuscript.

Competing interests

H.O. is a Guest Editor for *Communications Materials* and was not involved in the editorial review of, or the decision to publish, this Article. All other authors declare no competing interests.

Additional information

Supplementary information The online version contains supplementary material available at <https://doi.org/10.1038/s43246-024-00481-9>.

Correspondence and requests for materials should be addressed to Sai Kiran Rajendran or Hamid Ohadi.

Peer review information *Communications Materials* thanks Stephen Lynch and the other, anonymous, reviewer(s) for their contribution to the peer review of this work. Primary Handling Editor: Aldo Isidori. A peer review file is available.

Reprints and permissions information is available at <http://www.nature.com/reprints>

Publisher's note Springer Nature remains neutral with regard to jurisdictional claims in published maps and institutional affiliations.

Open Access This article is licensed under a Creative Commons Attribution 4.0 International License, which permits use, sharing, adaptation, distribution and reproduction in any medium or format, as long as you give appropriate credit to the original author(s) and the source, provide a link to the Creative Commons licence, and indicate if changes were made. The images or other third party material in this article are included in the article's Creative Commons licence, unless indicated otherwise in a credit line to the material. If material is not included in the article's Creative Commons licence and your intended use is not permitted by statutory regulation or exceeds the permitted use, you will need to obtain permission directly from the copyright holder. To view a copy of this licence, visit <http://creativecommons.org/licenses/by/4.0/>.

© The Author(s) 2024